

Velocimetry of cathode particles in a magnetoplasmadynamic thruster discharge plasma

J. Walker, S. Langendorf, M. Walker, K. Polzin, and A. Kimberlin

Citation: [Review of Scientific Instruments](#) **86**, 073513 (2015); doi: 10.1063/1.4927477

View online: <http://dx.doi.org/10.1063/1.4927477>

View Table of Contents: <http://scitation.aip.org/content/aip/journal/rsi/86/7?ver=pdfcov>

Published by the [AIP Publishing](#)

Articles you may be interested in

[Mode transition of a Hall thruster discharge plasma](#)

J. Appl. Phys. **115**, 203304 (2014); 10.1063/1.4879896

[One-dimensional hybrid-direct kinetic simulation of the discharge plasma in a Hall thruster](#)

Phys. Plasmas **19**, 113508 (2012); 10.1063/1.4768430

[Study of applied magnetic field magnetoplasmadynamic thrusters with particle-in-cell and Monte Carlo collision. II. Investigation of acceleration mechanisms](#)

Phys. Plasmas **19**, 073108 (2012); 10.1063/1.4737104

[Study of applied magnetic field magnetoplasmadynamic thrusters with particle-in-cell code with Monte Carlo collision. I. Computation methods and physical processes](#)

Phys. Plasmas **19**, 073107 (2012); 10.1063/1.4737098

[Self-heated hollow cathode discharge system for charged particle sources and plasma generatorsa\)](#)

Rev. Sci. Instrum. **81**, 02B305 (2010); 10.1063/1.3258033



 **SHIMADZU** Excellence in Science **Powerful, Multi-functional UV-Vis-NIR and FTIR Spectrophotometers**

Providing the utmost in sensitivity, accuracy and resolution for a wide array of applications in materials characterization and nanotechnology research

- Photovoltaics
- Polymers
- Thin films
- Paints/inks
- Ceramics
- FPDs
- Coatings
- Semiconductors

[Click here to learn more](#)



Velocimetry of cathode particles in a magnetoplasmadynamic thruster discharge plasma

J. Walker,^{1,a)} S. Langendorf,¹ M. Walker,^{1,a)} K. Polzin,² and A. Kimberlin²

¹*School of Aerospace Engineering, Georgia Institute of Technology, 270 Ferst Drive, Atlanta, Georgia 30332, USA*

²*Propulsion Research and Technology Applications Branch, NASA-Marshall Space Flight Center, Huntsville, Alabama 35811, USA*

(Received 12 March 2015; accepted 15 July 2015; published online 28 July 2015)

With high-speed imaging, it is possible to directly observe the time-evolution of the macroscopic behavior of the discharge plasma in a magnetoplasmadynamic thruster (MPDT). By utilizing direct high-speed imaging capable of capturing many images over the course of a single discharge, the velocity of the cathode erosion particles can be measured, opening the possibility of a novel, noninvasive technique for discharge plasma flow field velocimetry. In this work, an 8 kA argon MPDT discharge is imaged at 26 173 fps utilizing a 0.9 neutral density filter. The camera is aligned with thruster centerline 4 m downstream of the thruster exit plane. By tracking visible particles appearing in the multiple images, the particle motion in the radial and azimuthal directions is directly imaged. Through the use of traditional techniques in digital particle image velocimetry, the cathode particles emanating from the discharge are measured to have a mean radial velocity of 44.6 ± 6.0 m/s with a 95% confidence interval and a statistically insignificant azimuthal velocity. The setup and analysis employed permits measurement of the particle velocity in orthogonal direction to the image sensor plane using a single camera. By combining a background removal subtraction technique and knowledge of the optical focal plane, the estimated mean axial velocity of the particles is 1.59 km/s. This investigation ends with a discussion of important factors to consider for future MPDT high-speed imaging particle velocimetry, such as frame-rate, image size, spatial resolution, optics, and data handling selections. © 2015 AIP Publishing LLC. [<http://dx.doi.org/10.1063/1.4927477>]

I. INTRODUCTION

For the benefits of electric propulsion to be realized for human exploration or “fast” unmanned missions, plasma accelerator technologies must be able to handle power densities greater than what is feasible with current Hall effect thruster and ion thruster architectures. Magnetoplasmadynamic thrusters (MPDTs) are a viable candidate that can operate in the high-power regime at the high power densities necessary for such missions. In principal, a MPDT operating at MW power levels can achieve specific impulses over the range of 1700–4000 s at thrust levels in the 10 s of newtons.^{1–3} Experimental performance characterization at these power levels has identified fundamental problems regarding the discharge plasma stability and electrode erosion.^{1,2,4–8}

The MPDT is a coaxial-type plasma accelerator, and a generalized cross-sectional view of which is shown in Fig. 1. A center electrode, commonly referred to as the cathode, is constructed of a thermionically emissive material. The outer electrode, the anode, is concentrically placed around the cathode with a gap between the two electrodes. A voltage potential is established between the anode and the cathode to drive current within the discharge channel. When a plasma discharge is initiated, it serves to complete the electrical circuit between

the anode and cathode. The discharge is initiated by flowing propellant in the channel between the electrodes and then applying sufficient voltage between the cathode and the anode to ionize the gas in the gap, thus generating a plasma.^{1,2} The high current that flows as a result is often large enough to produce its own appreciable azimuthal magnetic field that interacts with the current to yield a “ $\mathbf{j} \times \mathbf{B}$ ” Lorentz body force. This kind of MPDT is often referred to as a self-field configuration as the magnetic field is both generated by and interacts with the discharge current. The axial component of the body force acts to directly accelerate the plasma out of the thruster.

For optimal performance and to minimize anode and cathode erosion, an azimuthally symmetric, uniform plasma discharge is desirable. However, with discharge currents on the order of 10 kA, a concentrated, localized arc structure can form. These arcs can arise through plasma instabilities, geometric asymmetries, or surface defects in the MPDT. Localized arc attachment to the cathode can produce significant heating and the ejection of cathode material in the form of large particles. As an example, enhanced thermal loading owing to localized arc attachment has been documented to enhance erosion rates of the cathode when a thruster is just starting and still cold. Arc attachment and localized thermal loading has been observed to produce average cathode erosion rates as high as $16.7 \mu\text{g}/\text{C}$ at start-up, while it is often $<0.2 \mu\text{g}/\text{C}$ during steady-state operation.^{9,10} Real-time measurements of cathode erosion in a MPDT have not previously been achieved; therefore, it has been unclear as to the overall distribution of

^{a)}Authors to whom correspondence should be addressed. Electronic addresses: jwalker30@gatech.edu and mitchell.walker@ae.gatech.edu

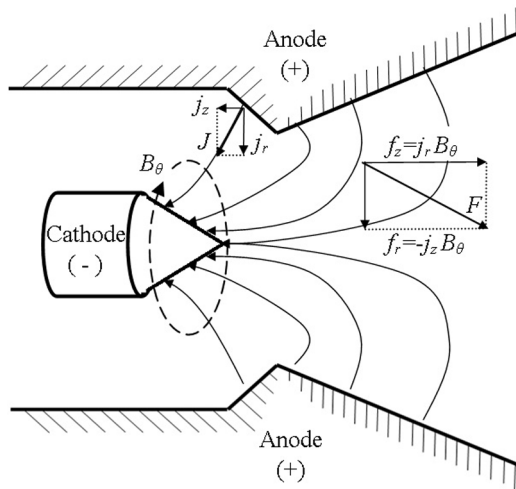


FIG. 1. Notional diagram showing basic MPDT operation. Not to scale.

sizes of cathode-sourced particles in the discharge plasma. However, due to the brittle nature of tungsten and the high thermal loading on the cathode, fragmentation and ejection of large particles of the cathode are possible.

Recently, Walker *et al.*¹¹ observed macroscopic particles in both high-speed and long exposure imaging and postulated that these particles emanate from the cathode. While that work did not focus on an analysis of the particles, it was observed that they appeared to have significant axial and radial velocities. In the present paper, we examine the visible particles in the high-speed images first presented in the work of Walker *et al.*,¹¹ using the images to quantitatively measure their velocities.

Past efforts to measure the flow-field in a MPDT have relied on laser induced absorption velocimetry.¹² These techniques have the benefit of being non-invasive to the flowfield and are able to precisely measure the velocity distribution of various species. Such techniques require line-of-sight between the laser source and the photo-multiplier tube. As MPDTs are typically coaxial-type devices, achieving line-of-sight within the thruster requires unusual thruster geometries and/or cut-outs in the sides of the thruster.¹²⁻¹⁴ While modifications to the physical geometry of the MPDT are not ideal and can introduce additional variations in an already complicated device, Kinefuchi *et al.*¹² reasoned and demonstrated that a 2-dimensional geometry would not introduce anomalous behavior from that of the typical coaxial accelerator.

The advent of high-speed imaging presents the opportunity for velocimetry measurements in a MPDT that are non-invasive to the flow field and do not involve modifications to physical geometry of the thruster. The present investigation is a proof-of-concept demonstration where digital particle image velocimetry (DPIV) is applied to the MPDT discharge plasma. In this case, the velocimetry uses already present cathode erosion particles as seed particles. Velocimetry information, gained from further refinements of this technique, may be helpful in understanding the underlying physical acceleration mechanisms in a MPDT discharge by providing valuable flow-field data necessary to validate current models. While the work presented in this paper is only a proof-of-concept, the demonstrated technique may be used in future MPDT testing, with

high-speed imaging used to obtain temporally and spatially resolved discharge plasma velocity flow-field measurements.

II. EXPERIMENTAL APPARATUS

In Secs. II A–II E, we give a brief overview of the facilities, experimental hardware, and data acquisition systems used to support the testing of a self-field MPDT operating near the critical current regime.

A. Vacuum chamber

All of the experiments are performed in the Vacuum Test Facility-2 (VTF-2) at the Georgia Institute of Technology. Fig. 2 shows a schematic of VTF-2 and the relative locations of the MPDT and diagnostics. VTF-2 is a 9.2-m long and 4.9-m diameter stainless steel chamber. It is evacuated to rough vacuum with one 3800 CFM blower and one 495 CFM (cubic feet per minute) rotary-vane pump. Ten liquid nitrogen cooled shrouded CVI TM-1200i re-entrant helium gas cycle cryopumps with a combined pumping speed of 620 000 l/s on argon bring the chamber to a base pressure of 6×10^{-9} Torr (measured on N_2). A Stirling Cryogenics SPC-8 RL special closed-looped nitrogen liquefaction system supplies liquid nitrogen to the cryopump shrouds.¹⁵ Two high-vacuum ionization gauges, a Varian model 571 and a Bayard-Alpert model UHV-24, are mounted on opposing sides of the chamber with a measurement uncertainty of $\pm 25\%$ of the indicated pressure for both ionization gauges.

B. MPD thruster

The thruster features a design similar to the MW-class thruster developed and tested at the NASA Glenn Research Center.^{2,16} The thruster is a self-field configuration, featuring a $3/4$ -in. thoriated tungsten center cathode, 2.5-in. wide by 2.1-in. length discharge channel, and a 3-in. thick stainless steel anode. A more detailed description of the NASA Glenn Research MPD thruster geometry can be found in the work of LaPointe and Pencil.¹⁶ The MPDT is designed to handle power levels above 1 MW in a pulsed firing configuration. Fig. 3 shows a detailed frontal view of the thruster assembly. Magnetic nozzle coils are wrapped around the nozzle of the thruster, but these coils were held at thruster body ground potential and not powered during the testing described in this paper.

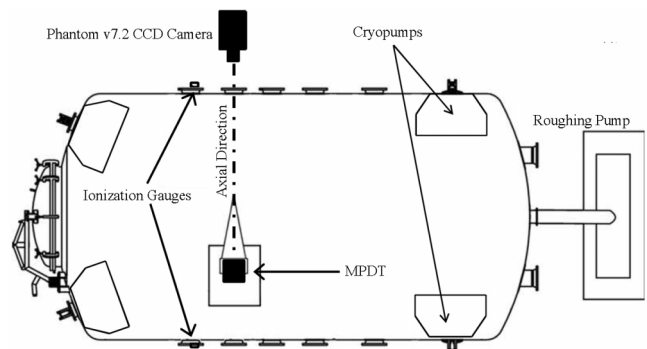


FIG. 2. Overhead view of the facility layout. Not to scale.

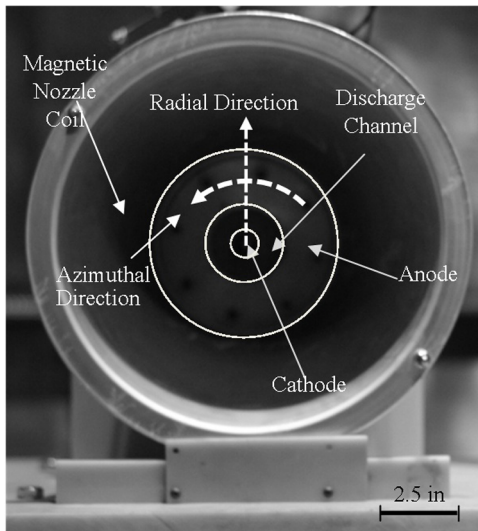


FIG. 3. Front view of thruster assembly. The magnetic nozzle coil windings are not visible in the image presented and are located behind the surface labeled “Magnetic Nozzle Coil.”

C. The pulse forming network (PFN)

Fig. 4 shows a schematic of the PFN used to power the discharge. The PFN consists of seven $360\text{-}\mu\text{F}$, 10-kV metalized-film capacitors with seven wound inductors connected in a Rayleigh line configuration. The total capacitance of the PFN is 2.52 mF with a maximum stored energy of 126 kJ . Because capacitors of equal size are used, the impedance of the PFN is high compared to other Guillemin-type networks that can have impedances on the order of the arc resistance $\sim 10\text{ m}\Omega$. The inductors are composed of wire (#2-AWG (American Wire Gauge)) wrapped around 24-in. diameter PVC piping, with the winding held in place by Lexan bracketing. The PFN features a custom built $200\text{-m}\Omega$ resistive ballast load and an emergency energy dump pathway. A hammer-type tungsten rod switching mechanism controls the PFN pulsing system. Circuit response simulations show that under the conditions listed above, the PFN can deliver an approximately flat-topped 10-kA pulse lasting for longer than 3.5 ms . Power is supplied to the MPDT through 2 pairs of 10 kV feedthroughs located on separate flanges.

D. Pulsed gas feed system

The thruster was designed to operate at mass flow rates greater than 0.3 g/s . Since these are high mass flow rates, a

pulsed gas feed system like that used in the work of LaPointe and Mikellides² was employed to maintain a facility operating pressure in the low 10^{-5} Torr range during testing. The system features a 678 in.^3 internal volume scuba tank rated to 3000 psi as a propellant plenum and an Omega SV251 3-way solenoid valve. A 0.0625-in. stainless steel tube serves as a choke in the system. The plenum is connected to a bottle of 99.999% purity argon and maintained at a desired pressure with a calculated pressure drop less than 0.02% during each gas pulse. Adjustment of the plenum pressure allows for control of the mass flow rate during a pulse. Using the calibration method outlined in the work of LaPointe and Mikellides,² a mass flow rate uncertainty of less than $\pm 5\%$ is expected. For a gas pulse duration of 1 s , the maximum expected background pressure during operation is between 7.8×10^{-6} and 1.5×10^{-5} Torr, corrected for argon and found using the following equation:

$$P_{ar} = P_b + \frac{P_s - P_b}{C_{argon}}, \quad (1)$$

where P_{ar} is the pressure corrected argon in units of Torr, P_b is the measured base pressure in units of Torr, P_s is the indicated pressure in units of Torr, and the correction factor C_{argon} is 1.29 .

E. Data acquisition and imaging

A Tektronix DPO4045 oscilloscope and a Pearson model 1330 current transformer were used to sample the discharge current profile. The bandwidth of the oscilloscope is 500 MHz and the maximum sampling rate is 2.5 GS/s . The current transformer has a maximum measurable peak current of 100 kA and a useable rise time of $0.25\text{ }\mu\text{s}$. To ensure that the current measured accurately reflects the actual discharge current, the measurement is performed very near to the thruster with the current transformer located in the vacuum chamber 1 m from the thruster (see Fig. 5).

A Tektronix DPO7354C oscilloscope was used to sample the voltage of both the anode and cathode relative-to-ground. The bandwidth of the oscilloscope is 3.5 GHz , acquiring 12-bit data at a maximum sampling rate of up to 40 GS/s . The differential voltages between the electrodes and ground are measured using two Tektronix P6015A $1000:1\text{ 1 MHz}$ bandwidth high-voltage probes. These probes are located on the atmosphere side of the power feedthrough flange as shown in Fig. 5 because the voltage probes are not vacuum compatible. The overall voltage across the thruster is calculated as the difference between the two voltage measurements.

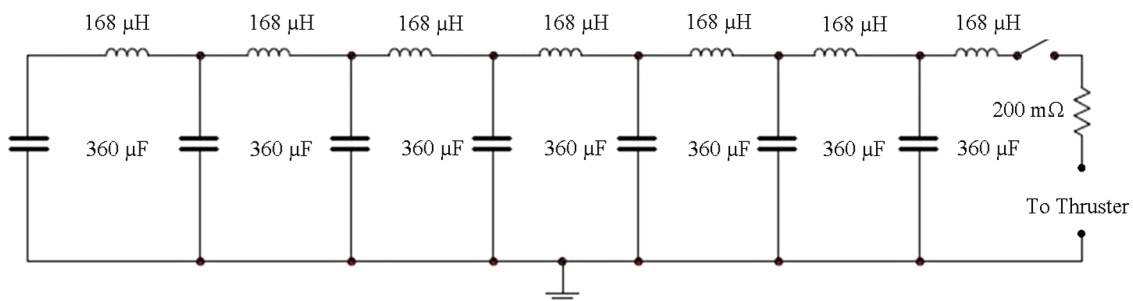


FIG. 4. Electrical schematic of the PFN. The $200\text{ m}\Omega$ resistive ballast load and is shown on the right-hand side.

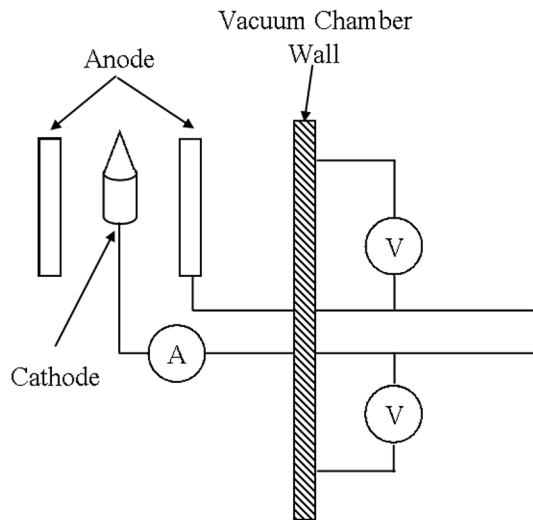


FIG. 5. Electrical diagnostic schematic showing the current and voltage diagnostic measurement points relative to the MPDT.

The current monitor and both voltage probes have an instrument uncertainty of $\pm 1\%$ of the measured value. Based on simulated discharges of the PFN and experimental results from Refs. 2, 3, 14, and 17, this data acquisition system can resolve features in the 1 MHz frequency range, which is more than sufficient to capture the discharge voltage and current profiles during thruster operation.

A Phantom v7.2 high-speed camera was used to image the discharge. The frame rate was set to 26 143 fps, yielding a maximum image size of 256×256 pixels. The camera is aligned axially with the MPDT, with a 12-in. diameter Lexan viewport providing optical access to the thruster during testing as shown in Fig. 2. The distance between the camera front lens element and the MPDT discharge channel exit plane was 4.00 ± 0.02 m. The lens has a calculated focal length of 130 mm and an f-stop number of 11. During some thruster pulses, a 0.9 neutral density filter is used to view the overall light emission of the thruster. On separate thruster pulses, instead of the neutral density filter, a 488-nm line filter with a 10-nm bandwidth (corresponding to an argon ion spectral emission line) was used to capture light emission from the thruster. All high-speed data systems are triggered on the initial current rise as measured by the current transformer.

III. EXPERIMENTAL RESULTS

Before beginning the analysis of the imaged particles, it was necessary to demonstrate that the MPDT was operating nominally and verify that the particles seen in the imaging were indeed sourced from the cathode. In the first part of the present section, experimental results from the thruster operating at nominal condition are presented. A brief comparison is made to previously published data on this thruster to establish that it is operating as intended. In the second part of this section, the imaging is examined to determine if concentrations of light that appear in the images represent cathode sourced particles. To do this, it is first verified through a background removal process that these concentrations of light are not artifacts of the imaging. Then, the images acquired using a neutral density

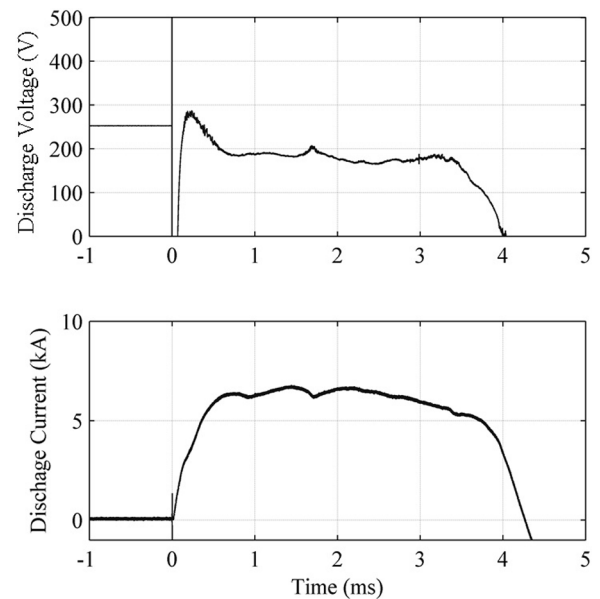


FIG. 6. Nominal MPDT operation showing voltage drop between the cathode and the anode (top) and current (bottom) waveforms for a mass flow rate of 0.36 g/s.

filter and a 488 nm notch filter are compared. In doing so, it is confirmed that these concentrations of light are not due to any local concentrations of discharge plasma.

A. Quasi-steady state thruster operating condition

The nominal operating condition of the MPDT for all of the imaging presented in this paper is an 8 kA discharge current with a mass flow rate of 0.36 g/s of argon. Fig. 6 is waveforms of the quasi-steady-state voltage and current delivered to the thruster by the PFN. The absence of high-frequency voltage oscillations is a clear indication that the thruster was operating below the so-called “onset” condition. In comparison to other experiments utilizing this MPDT design, the voltage drop across the cathode is approximately 128 V higher than what has been previously observed.² This voltage difference is due to the PFN impedance, which is much higher than the impedance of the PFN utilized at NASA GRC.

B. Observed cathode particulates in the discharge

To aid in the discussion of the imaging, a coordinate system for the thruster is shown in Figs. 2 and 3. The axial direction is defined as aligned with the centerline of the thruster and pointed downstream. The radial direction origin is fixed on the thruster centerline, with the azimuthal direction being around the centerline. Imaging performed using the neutral density filter during MPDT operation revealed concentrated regions of light forming near the exterior edge of the discharge channel and propagating radially towards the outer edge of the anode. An examination of the imaging aimed at determining if the concentrations of light are indeed particles sourced from the cathode is described below.

As shown in Fig. 7, the concentrations of light are difficult to see against the background of the plasma discharge in the raw imaging. To help in enhancing the contrast between these concentrations of light and the plasma discharge,

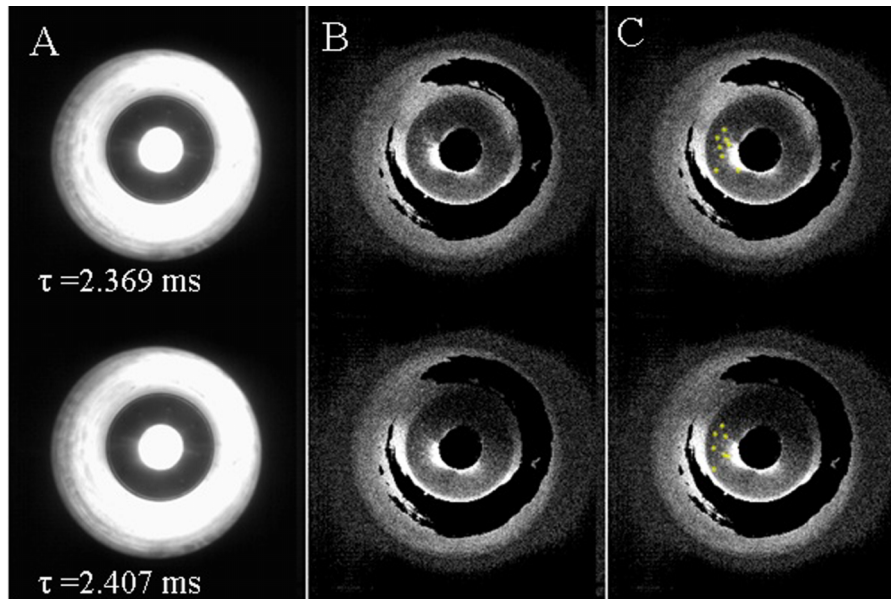


FIG. 7. MPDT discharge image processing for two different times showing: (a) raw unprocessed images, (b) images after application of the background removal process, and (c) the same image in (b) with particles identified and highlighted by yellow dots.

a background subtraction algorithm commonly used in digital particle interference velocimetry is applied.¹⁸ In this process, a local pixel intensity temporal minimum value is established for each pixel. The pixel minimum is the lowest pixel intensity observed in the frames before and after the frame undergoing the background subtraction process for the respective pixel. Once the local minimum is established for each pixel, the local minimum value is then subtracted from the current pixel values. This technique can remove slow moving particles from the imaging if the time window is not large enough to capture the movement of the particle. It is therefore necessary to tune the length of the time domain for the minimum pixel intensity throughout the imaging to avoid the deletion of slow moving particles, increase the contrast between the concentrations of light, and minimize the introduction of noise. The results of this processing effectively remove the static background of the image, including much of the quasi-steady plasma discharge light emission. Fig. 7 shows results of this processing technique applied to two images that were acquired using the neutral density filter. In this imaging, concentrated regions of light between 1 and 3 pixels in diameter can be seen propagating radially from the discharge channel. These areas are highlighted in the final figure on each row. Once

the concentrated regions of light appear in the imaging, they move outward radially. These concentrations of light appear at random time intervals, which is to be expected if these concentrations of light are in fact cathode-sourced particles. Tracing the trajectory of these particles leads to a source within the discharge channel. However, these concentrations of light cannot be seen within the discharge channel since the light there fully saturates the camera to a maximum pixel value intensity of 255. When the background subtraction process is applied to this region, all that remains is the black central circle in the second and third images on each row in Fig. 7, making it impossible to identify anything else in the channel.

To ensure that these concentrations of light are not due local concentrations of discharge plasma, background removal process was applied the second time to the images acquired using the 488-nm argon ion line filter. In this processing, unlike in Fig. 7, the images contained no similar concentrations of light propagating radially outward from the discharge channel region. This absence implies that the propagating concentrations of light seen in Fig. 7 are not argon plasma. Based on the trajectory of these light concentrations after they exit the discharge region and the significant erosion of the cathode, as seen in the pre- and post-test images in Fig. 8, it is claimed

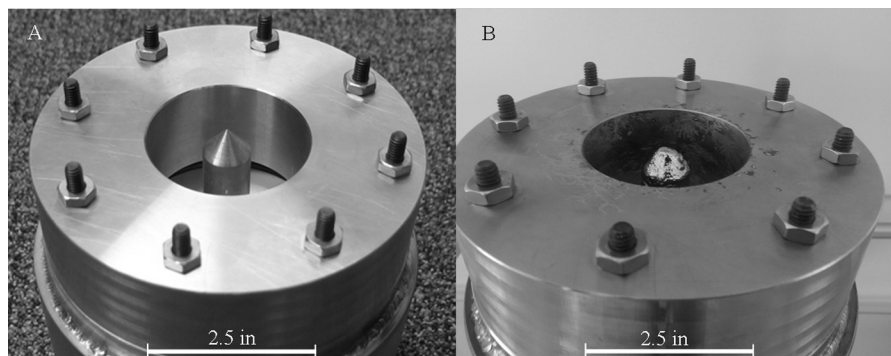


FIG. 8. Picture of MPDT (a) before and (b) after several pulses, showing the effects of erosion on the cathode (central electrode).

that these moving concentrations of light are particles that have been ejected from the cathode.

IV. VELOCITY MEASUREMENTS

Sections IV A and IV B detail the analysis of the post-processed images using velocimetry on the cathode particles. The velocity analysis is split into two sections: radial-azimuthal velocimetry and axial velocimetry.

A. Radial and azimuthal particle velocimetry

The head-on orientation of the camera to the MPDT makes radial and azimuthal particle velocity tracking a straight-forward process where we simply follow the particles across the imaged area from one frame to the next. To accomplish this tracking, the particles must be identified in each frame and then correlated or matched to observed particles in temporally adjacent frames. In doing so, the trajectory of the particle can be traced frame-by-frame to calculate the velocity. Two separate data extraction and particle velocity measurement techniques are compared in this section and exhibit quantitative agreement regarding the measured average particle velocities.

Attempts to use algorithms to automatically identify particles against the background failed because the particle density and contrast were too low for reliable, repeatable particle identification. Because of this limitation, each particle was identified manually in every frame. An open-source MATLAB tracking library based on the IDL (Interactive Data Language) particle tracking software is used to correlate the particles between frames. The tracking library is based on the mathematical algorithms described in the work of Crocker and Grier.¹⁹ In the tracking process, particles in each frame are matched with corresponding particles in subsequent frames, yielding particle trajectories over time. The tracked particles have a diameter on the order of 1.6 μm or smaller. The radial components of the velocity are calculated directly by taking the particle displacement per frame and dividing by the time step. After removal of the statistical outliers, taken as values exceeding 1.5 times the interquartile range of the data, this method yields an average radial particle velocity of 50.2 m/s with a standard deviation of 10.0 m/s. The standard deviation is the classically defined range around the mean that encompasses 68.2% of the data. The azimuthal velocity was measured to be 19 m/s with a standard deviation of 11.8 m/s. An azimuthal particle velocity measured in meters per second includes errors associated with both the radial and azimuthal positional accuracy of the particle's centroid. To decouple the positional error associated with the radial and azimuthal particle centroid location, the azimuthal particle velocity is then calculated in radians per second. The azimuthal particle velocity in radians per second is measured to be 487 rad/s with a standard deviation of 315 rad/s. At the given frame rate, a 487 rad/s azimuthal velocity corresponds to a position change of 18.6 mrad or 1.06° between frames. This change in angular position is small enough that slight variations in where the particle centroid is identified make it difficult to accurately determine the frame-to-frame azimuthal velocity.

While the large standard deviation implies a wide range of azimuthal velocities, these changes are all still quite small, with the largest azimuthal velocity, 802 rad/s, measured, corresponding to an azimuthal position change between sequential frames of less than 1 pixel. By way of comparison, the much larger radial frame-to-frame position change can be as high as 3 pixels. The azimuthal velocity corresponds to a positional change in the sub-pixel range. This small change in position can be accurately correlated to a velocity with the particle tracking library; however, it is difficult to quantify the positional uncertainty of the particle's centroid location. If it is assumed to be 1 pixel, the frame-to-frame azimuthal velocity uncertainty is greater than the measured azimuthal velocity for all particles. This investigation includes the azimuthal velocity measurement because the analysis techniques using particle centroids and the particle tracking library are capable of correlating subpixel displacements to a velocity.

The particle tracking software can only achieve consistent results by assuming *a priori* knowledge of the maximum particle displacement between frames to correlate individual particles across several frames. With this limitation in mind, velocity measurements were performed in a second way as a check to verify that the azimuthal and radial velocities found in the previous paragraph are of the correct order of magnitude. Fig. 9 shows the radial positions of many particles for a subset of the total imaging time. Using a least squares linear regression fit of the data, the calculated slope of the regression is taken to correspond to the average particle velocity. The limitation of this regression method is that in order for the slope to correspond to the particle velocities, the regression must be done on the same group of particles over time. Consequently, the accuracy of this method depends heavily on the ability to track a group of particles. Without *a priori* knowledge of the particles' trajectories, it is difficult to correlate a specific particle over subsequent frames and establish a fixed group of particles to follow. Since the goal of this second technique is to try to measure the group particle velocity without the use of *a priori* knowledge of the particle trajectories, the linear regression is applied to all particles appearing during a small subset of the imaging time. Since these particles originate from

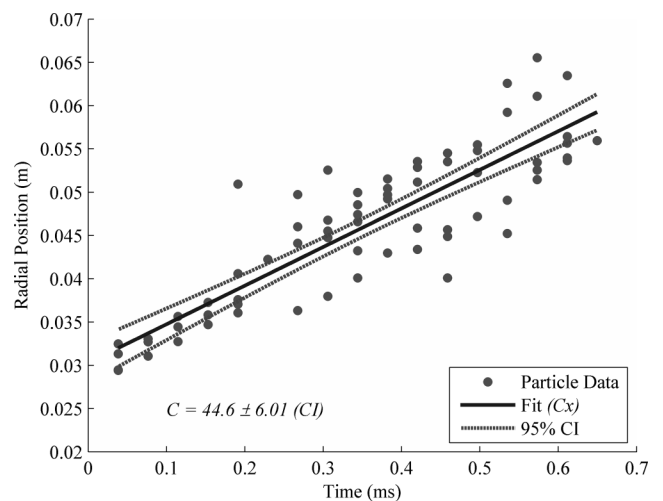


FIG. 9. Radial particle position as a function of time. Data are shown for a subset of the particles identified in the imaging.

the cathode, new particles appearing at later times will artificially lower the slope of the regression. To aid in understanding the statistical and physical meaning of the linear regression fit, it is necessary to review certain principles of linear regression. In this method, the slope of the regression is used to statically estimate the velocity of the particles imaged. As the slope is a statistically calculated estimate, the linear regression slope represents a statistical random variable with an assumed normal distribution of a mean and standard deviation. Because of this, it is possible that the linear regression is a result of random happenstance and not statistically significant.

As a means of measuring the statistical significance, the 95% confidence interval is utilized; if one were to repeat the linear regression on statistically similar data, the calculated slope would fall within the confidence interval 95% of the time. In measuring the statistical significance of the linear regression slope, a 95% confidence interval that does not include a zero crossing means that the linear regression slope is non-trivial and therefore statistically significant. It is also interpreted that the confidence interval of a linear regression slope gives a range of statistically likely values. To avoid confusion, it is important to note that the slope confidence interval and the linear regression confidence interval shown as dashed lines in Figs. 9 and 10 are fundamentally two different quantities. The confidence interval for the linear regression fit is representative of the ability of the linear model to statistically predict the data. As such, the width of the linear regression confidence interval is the smallest close to the arithmetic mean of the data. The width of this confidence interval grows larger towards the dataset maximum and minimum. The measured radial velocity via the regression is 44.6 m/s with a ± 6.0 m/s 95% confidence interval. Comparing the radial velocity measured via the particle tracking library approach and the linear regression in Fig. 9, we find that the two do, within the confidence intervals, exhibit quantitative agreement. Fig. 10 shows that the linear regression process applied to a small group of particles moving in the azimuthal direction yields an azimuthal velocity of 237 rad/s with a ± 45 rad/s with a 95% confidence interval. This group of particles is smaller than that used in the radial velocity

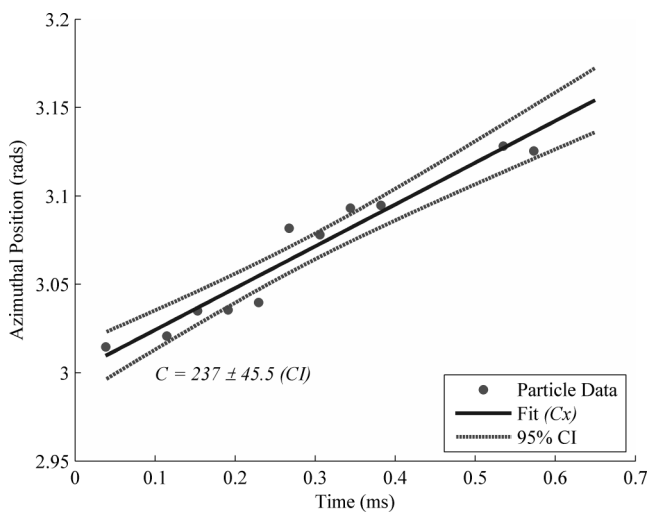


FIG. 10. Azimuthal particle position as a function of time shown for a subset of the particles identified in the imaging.

linear regression because the small angular position changes of the particles produced only slight variations in their centroid locations and led to trivial linear regression fits. The group of particles shown in Fig. 10 represents a small sub-sample of particles detected that led to a non-trivial regression fit. Comparison of the azimuthal particle velocities found using the two methods again find good quantitative agreement.

B. Axial velocimetry of cathode particles

The orientation of the camera relative to the thruster does not allow for measurement of the axial velocity of the particles by tracking their movement across the picture. However, an estimate of the axial velocity of some particles is possible by examination of a certain class of particles. To better understand how this estimate is performed, the effect of the background removal process on particles moving outside of the depth-of-field of the optics is first considered. As the particles traverse downstream, they will at some point pass through an axial position where, given the optics of the camera, they are no longer in focus. As the particles pass through the focal plane, their images will blur with the light continuing to spread over a larger area on the sensor until it simply becomes an indistinguishable part of the background light. If the radial velocity of the particles is small relative to the axial velocity, they will disappear from the image not because they traversed the radial distance across the anode face but because they have translated axially through the focal plane. The further these particles are located from the focal plane of the optics, the more their light becomes blurred into the background of the image. The background removal process enhances the removal of these particles. Since the focal plane of the lens has fixed spatial thickness, the number of frames it takes before a particle traverses this distance and is out of sight can be correlated to a velocity. The boundaries of this focal plane, past which the particles become sufficiently defocused to be removed from the imaging, is not known precisely, but can be estimated using the classical focal plane optics relations,²⁰

$$H = \frac{f^2}{Nc} + f, \quad (2)$$

$$D_n = \frac{s(H-f)}{H+s-2f}, \quad (3)$$

$$D_f = \frac{s(H-f)}{H-s}, \quad (4)$$

where H is the hyperfocal distance in units of mm, f is the focal length in units of mm, N is the F-stop aperture number, c is the diameter of the airy disk for the lens and camera used in units of mm, s is the distance to the object in units of mm, D_n and D_f are the focal plane near and far limits respectively in units of mm. The calculated depth of field near limit D_n and far limit D_f are 3.85 m and 4.16 m, respectively. Thus, the depth of the focal plane is 0.31 m. While the precise location of the focal plane was not measured for this particular set of tests, the lens is focused such that the cathode, anode face, and interior of the discharge channel are sharply resolved. Consequently, we take this position as being the far limit on the focal plane, with an overall depth of field through which resolved particles can travel being 0.26 m, which is the size of the focal plane minus

the depth of the discharge channel. This limit in focal plane size subsequently places a 3400 m/s limit on the maximum axial velocity measurable with this technique.

Because of the specific requirement that the particles exit the image through axial instead of radial motion, only a select number of particles imaged are viable candidates for the use of this technique. In total for the dataset analyzed, only six particles meet the special requirements for this technique to be applicable. The mean of the axial velocity measured in this way was 1590 m/s with the maximum and minimum velocities being 2270 m/s and 1130 m/s, respectively. These particle velocities are within the range of possibility for the plasma discharge of a MPDT operating at 8 kA of discharge current.^{1,21} What has been demonstrated is a viable proof-of-concept measurement technique that gives an estimate of axial particle velocity that would have been otherwise unattainable.

V. DISCUSSION

In this section, we present lessons learned and critical points of consideration to aid future experiments seeking to perform velocimetry measurements via the methods described in this investigation.

A. Camera

The camera selection is one of the most important elements when implementing the velocimetry setup described in this paper. For a given high speed imaging camera, there is a trade-off between frame rate and image size. The optimum condition involves a camera that when operating at a fast frame rate still has enough spatial resolution to observe frame-to-frame particle motion. As an example, the Phantom v7.2 camera used in this experiment had an imaged area of 256×256 pixels, which at the distance of the thruster corresponded to a spatial resolution of 1.06 mm/pixel. This places a lower bound both on the size of particles and the minimum particle motion that could be resolved. In this work, the radial particle velocity is on the order of 50 m/s, which at 26 173 fps implies that the particle displacement of no more than 1-2 pixels per frame.

The decision between utilizing a camera capable of color imaging and a monochromatic camera can impact the intensity of light reaching the CCD. While a CCD or complementary metal-oxide sensor has variable quantum efficiency, depending on the wavelength of the light incidence on the sensor, an individual pixel element cannot measure the wavelength and instead only records the intensity of the light. To achieve color imaging, a “red, green, green, blue” filter pattern, also known as a Bayer filter, is overlaid directly onto the sensor. The filter decreases the light reaching the sensor in two ways. First, the color filter attenuates light at other wavelengths outside the color bandwidth. Second, the effective number of pixels measuring the light is reduced as different pixels are dedicated to different wavelengths of light. As an example of the decrease in the sensitivity, the Phantom v7.2 has a monochromatic sensor film-equivalent speed of ISO 4000 but it only has a color film-equivalent speed of ISO 1000. That difference translates into a factor of four reductions in light sensitivity. Since the Bayer filtering is applied at the hardware

level, the light sensitivity difference can only be compensated by adjusting the sensor gain through the ISO speed setting, thus reducing the dynamic range of the camera. Consequently, a monochromatic image sensor is recommended to accurately capture spatially and temporally resolved frames showing the discharge particles. Other camera related hardware criteria may be important in the selection process, but ensuring that the camera has a viable frame rate and image resolution and taking into account whether or not color imaging is necessary are the crucial factors to successfully performing high-speed imaging particle velocimetry of the MPDT discharge.

B. Imaging optics

The selection of a lens is important when attempting to resolve features within a MPDT discharge. Several camera lens properties can affect the overall quality of the captured image. The primary properties to consider in the present setup are the chromatic aberration and focal length of the lens. Chromatic aberration causes multiple images offset from each other to appear in a color image while it results in a blurring of features in a monochromatic image. This blurring is a consequence of the refractive index of the material having a dependence on the wavelength of the incident light, therefore making the focal distance of the lens dependent on the wavelength received. Such blurring will increase the uncertainty in the velocimetry techniques by making it more difficult to accurately determine the location of the particles in any frame. There are techniques that can be employed to overcome chromatic aberration, such as using ultra-low dispersion lens elements or an advanced optical design. To avoid the added uncertainty chromatic aberration would introduce in the velocimetry measurements, it is strongly advised to choose lenses that specifically have additional elements to deal with chromatic aberration. If this is not possible then a reduction in the aperture size will also reduce the image defects due to the optics, but this will also reduce the amount of light collected, decreasing the overall sensitivity.

Issues related to the focal length become important when performing velocity measurements that rely on knowledge of the location of the focal plane. Lenses have the inherent property of an infinity focus distance, defined as the distance beyond which all objects are in focus. As the focal length is decreased, the infinity focus distance of the lens also gets smaller. The advantage of using a smaller focal length is that the imaging incorporates a larger viewing angle. However, if the MPDT is placed beyond the infinity focus distance for that focal length, then the particles may always be in focus throughout the discharge pulse and, consequently, the defocusing technique used to measure the axial particle velocity may not be applicable. The center of the focal plane may also add uncertainty to the axial velocity measurement. If the camera and a telephoto lens have a compatible electronic interface, the location of the center of the focal plane and/or the size of the focal plane may be digitally recorded with the image itself. While some camera/lens combinations automatically adjust the focus and focal length, many experimentalists prefer to utilize a lens that has full manual control of the focal length, focus distance, and aperture. These manual lenses are

of benefit because they have a finely graduated focal length and the focus distance adjustments on the lens body and are continuous, as opposed to being stepped or discrete.

C. Image acquisition and processing

It is important that careful consideration be given to how the data are acquired when using high-speed imaging in the manner described in this paper. A poor choice in bit depth or video format can result in valuable information being lost through image compression. At the hardware level, pixel light intensity quantization commonly occurs at 14 bit. In order to reduce file size, many common video formats such as h.264 or MPEG-4 offer only 8 bits of quantization per color channel. Consequently, subtle details in the image are compressed, and those details appear more decentralized and spatially dispersed. When performing the background subtraction process as previously described, the loss in information due to data compression from 14 bit to 8 bit can result in loss of particles, spatial resolution, and increased noise floor. In this proof of concept work, the image processing occurred at 8 bits. After the background subtraction process as shown in Fig. 7, the 8-bit depth led to an increased noise floor in comparison to the original image and a loss in particle sensitivity, such that only the particles emitting the most light are detected.

While the processing of the imaging at the 14-bit level is more resource intensive, the gains in sensitivity lead to better particle detection and tracking. To preserve information throughout the data processing routine, it is vital to choose a file format that will not compress the image. Common video codecs such as h.264, MPEG-4, AVCHD, and ProRes422 all perform image compression in the form of bit depth reduction and variable image quality. These compression algorithms can result in aliasing and reduction in spatial resolution. To avoid this problem, it is necessary to carefully consider the high-speed camera image output formats and choose one that is lossless, such as Digital Negative (DNG) or uncompressed tagged image file format (TIFF). If such an option is not available, then using raw images output by the camera sensor may be a possible alternative. In a raw image, the sensor pixel intensity values are saved with a bit depth based on the available hardware quantization. For both color and monochromatic imagings, this information is not readily accessible for post-processing and requires a file conversion or de-Bayering. In a Bayer filter image each pixel only measures the intensity of one color. De-Bayering is an algorithmic technique that determines the other two color values for each pixel by estimating each pixel's red, green, and blue (RGB) values using data from neighboring pixels. The actual de-Bayering algorithm varies depending on desired spatial resolution and available compute time. Therefore, careful consideration must be made when selecting a de-Bayering algorithm for post-processing of raw chromatic image sensor data to avoid unwanted decreases in spatial resolution or aliasing in high speed color imaging.

VI. CONCLUSION

In this work we employed high-speed imaging to perform direct, global imaging of the macroscopic behavior of the

MPDT discharge plasma. An analysis of the images was performed to demonstrate a novel velocimetry technique where the 3-dimensional velocities of particles emanating from the cathode in an MPDT discharge were measured utilizing a single camera. The method to determine particle radial azimuthal velocities was dependent upon the spatial and temporal resolution in the images, while particle motion along the thruster axis was estimated using knowledge of the location of the optical focal plane. The mean radial velocity of particles was found to be 44.6 ± 6.0 m/s within a 95% confidence interval, while the azimuthal velocity was statistically insignificant. The mean axial particle velocity was measured as 1.59 km/s. The effects of imaging factors such as camera selection, collection optics design, and principle photographic settings were discussed with suggestions as to the proper choices for each provided. The particle tracking and measurement techniques described in this paper are potentially useful in future studies, as a measure of particle velocity may serve as a way to perform a non-invasive proxy measurement of the gasdynamic MPDT flow-field.

ACKNOWLEDGMENTS

J. A. Walker would like to thank the National Science Foundation Graduate Research Fellowship Program for funding that enabled this research to be accomplished. We are grateful for the efforts of Nicole Tyman and Joshua Mann for their assistance in the installation and operation of the MPDT support facilities.

K. A. Polzin and A. C. Kimberlin acknowledge NASA Marshall Space Flight Center (MSFC) management support from Jim Martin, J. Boise Pearson, Mary Beth Koelbl, Thomas Williams, and Paul Mcconnaughey. We are grateful to Craig Garrison of NASA-MSFC for the loan of the Phantom v7.2 camera that made this work possible.

¹R. G. Jahn, *Physics of Electric Propulsion* (Courier Dover Publications, New York, New York, 2012).

²M. LaPointe and P. Mikellides, "High power MPD thruster development at the NASA Glenn Research Center," in 37th Joint Propulsion Conference and Exhibit, Salt Lake City, Utah, 8–11 July 2001.

³M. R. LaPointe, "Numerical simulation of cylindrical, self-field MPD thrusters with multiple propellants," in International Electric Propulsion Conference, Seattle, Washington, September 1993.

⁴J. L. Lawless and V. Subramaniam, "Theory of onset in magnetoplasmadynamic thrusters," *J. Propul. Power* **3**, 121 (1987).

⁵K. A. Polzin, T. E. Markusic, R. L. Burton, R. E. Thomas, and D. L. Carroll, "Gallium electromagnetic (GEM) thruster concept and design," in 42nd Joint Propulsion Conference and Exhibit, Sacramento, CA, 9–12 July 2006.

⁶R. Thomas, R. Burton, and K. Polzin, "Investigation of a gallium MPD thruster with an ablating cathode," in 46th AIAA/ASME/SAE/ASEE Joint Propulsion Conference and Exhibit, Nashville, TN, 25–28 July 2010.

⁷H. O. Schrade, M. Auweter-Kurtz, and H. L. Kurtz, "Stability problems in magnetoplasmadynamic arc thrusters," *AIAA J.* **1633**, 10 (1985).

⁸R. E. Thomas, R. L. Burton, and K. A. Polzin, "Performance characteristics of an ablative gallium electromagnetic accelerator," *J. Propul. Power* **29**, 930 (2013).

⁹H. O. Schrade, M. Auweter-Kurtz, and H. L. Kurtz, "Cathode erosion studies on MPD thrusters," *AIAA J.* **25**, 1105 (1987).

¹⁰R. G. Jahn and E. Y. Choueiri, in *Encyclopedia of Physical Science and Technology*, 3rd ed., edited by R. A. Meyers (Academic Press, New York, 2003).

¹¹J. Walker, S. Langendorf, M. L. R. Walker, K. A. Polzin, and A. Kimberlin, "High-speed imaging of the first kink mode instability in

- a magnetoplasmadynamic thruster,” in International Electric Propulsion Conference, Washington DC, USA, 6–10 October 2013.
- ¹²K. Kinefuchi, I. Funaki, and K. Toki, “Laser absorption velocimetry of plasma flow in two-dimensional magnetoplasmadynamic arcjet,” *J. Propul. Power* **22**, 1085 (2006).
- ¹³P. Fabrizio, A. Mariano, A. Matteo, A. Vanni, Z. Matteo, S. Gianluca, M. Piero, B. Federica, F. Paolo, M. Bagatin, R. Cavazzana, L. Marerelli, E. Martines, R. Rossetti, M. Signori, G. Serianni, and P. Scarin, “Further experimental evidences of the development of kink instabilities in MPD thrusters,” in 41st AIAA/ASME/SAE/ASEE Joint Propulsion Conference and Exhibit, Tucson, Arizona, 10–13 July 2005.
- ¹⁴F. Paganucci, M. Zuin, M. Agostini, M. Andrenucci, V. Antoni, M. Bagatin, F. Bono, R. Cavazzana, P. Franz, L. Marrelli, P. Martin, E. Martines, P. Rossetti, G. Serianni, P. Scarin, M. Signori, and G. Spizzo, “MHD instabilities in magneto-plasma-dynamic thrusters,” *Plasma Phys. Controlled Fusion* **50**, 124010 (2008).
- ¹⁵A. Kieckhafer and M. L. R. Walker, “Recirculating liquid nitrogen system for operation of cryogenic pumps,” in 32nd International Electric Propulsion Conference, Wiesbaden, Germany, 11–15 September 2011.
- ¹⁶M. LaPointe and E. J. Pencil, “NASA GRC high power electromagnetic thruster program,” in Space Technologies and Applications International Forum, Albuquerque, NM, 8–12 February 2004.
- ¹⁷M. Zuin, R. Cavazzana, E. Martines, P. Rossetti, M. Signori, M. Andrenucci, and M. Paganucci, “Investigation of MHD instabilities in an applied field MPD thruster by means of measurement of magnetic field fluctuations,” in International Electric Propulsion Conference, Ann Arbor, MI, 20–24 September 2009.
- ¹⁸*Encyclopedia of Microfluidics and Nanofluidics*, edited by D. Li (Springer US, 2008).
- ¹⁹J. C. Crocker and D. G. Grier, “Methods of digital video microscopy for colloidal studies,” *J. Colloid Interface Sci.* **179**, 298 (1996).
- ²⁰A. R. Greenleaf, *Photographic Optics* (Macmillan, Michigan, 1950).
- ²¹E. Choueiri, “On the thrust of self-field MPD thrusters,” in Proceedings of the 25th International Electric Propulsion Conference, Cleveland, OH, August 1997.